



Corrugated mesh flow channel and novel microporous layers for reducing flooding and resistance in gas diffusion layer-less polymer electrolyte fuel cells

Shiro Tanaka ^{a, b, *}, Toshio Shudo ^a

^a Department of Mechanical Engineering, Tokyo Metropolitan University, 1-1 Minami-Osawa, Hachioji, Tokyo 192-0397, Japan

^b HySA/Catalysis, Department of Chemical Engineering, University of Cape Town, Private Bag X3, Rondebosch, Cape Town 7701, South Africa

HIGHLIGHTS

- Large flooding reduction was attained with corrugated mesh in a GDL-less fuel cell.
- Flow-channel patterns affect the contact resistance of corrugated mesh MPLs.
- MPL conductivity is the key to reducing HFR without GDLs.
- MPL rigidity can affect contact resistance with improved pressure distribution.

ARTICLE INFO

Article history:

Received 18 November 2013

Received in revised form

13 February 2014

Accepted 29 April 2014

Available online 15 June 2014

Keywords:

Polymer electrolyte fuel cell

GDL-less

Flooding

Corrugated mesh flow field

Microporous layer

High-frequency resistance

ABSTRACT

Electrode flooding at the cathode impedes the increase in power density of polymer electrolyte fuel cells (PEFCs), limiting their use at high current densities. Liquid water can accumulate in the pores of the gas-diffusion layer (GDL), deteriorating performances significantly. This paper reports a novel fuel-cell structure for the reduction of electrode flooding utilizing corrugated mesh as gas-flow channels and gas diffusers placed directly onto the microporous layer (MPL) without a conventional GDL in between. The polarization curve of the corrugated-mesh fuel cell shows a lower flooding tendency at a high current density; however, the high-frequency resistance (HFR) of this fuel cell increases significantly as a result of fewer contact points between the corrugated mesh and MPL. In addition, MPL conductivity and rigidity are investigated in efforts to reduce the flow-channel pattern resistance. The rigidity of the MPL has a small effect on the reduction in HFR, which may be caused by an improved pressure distribution on the catalyst layer.

© 2014 Elsevier B.V. All rights reserved.

1. Introduction

Polymer electrolyte fuel cells (PEFCs), which convert the chemical energy of hydrogen directly into electrical energy, are regarded as a promising alternative technology and clean power source for automotive, stationary, and portable applications [1–5]. The utilization of fuel cells for powering automotive equipment requires a reduction in cost and size, as current automotive fuel cells are not profitable and are still too large, limiting the layout of the fuel-cell system [6].

Currently, most automotive fuel cells operate with a maximum current density of 1.0 A cm^{-2} [7–9]. This low current density requires a large active area in order to produce a vehicle power output of 70–120 kW, which consequently increases the number of polymer electrolyte membranes (e.g., Nafion, Acipex, and Dow membranes), catalyst layers with precious metals, and gas-diffusion layers (GDLs) required. The expense of these materials means that larger active areas significantly increase the cost of the fuel-cell stack. In addition, a GDL thickness of 90–200 μm for each electrode increases the length of the stacking direction, with the total volume of the GDL occupying about half of the fuel-cell stack. These considerations create limitations for conventional fuel-cell structures with regard to cost and size.

Solving these commercialization issues for automotive fuel cells requires a novel fuel-cell structure that enables high current density operation without a GDL. Increasing the current density of

* Corresponding author. HySA/Catalysis, Department of Chemical Engineering, University of Cape Town, Private Bag X3, Rondebosch, Cape Town 7701, South Africa. Tel.: +27 21 650 3852; fax: +27 21 650 5509.

E-mail address: shiro.tanaka@uct.ac.za (S. Tanaka).

conventional fuel cells causes a sudden decrease in performance, known as cathode flooding. When current density increases, more water is generated in the electrochemical reaction ($\text{O}_2 + 4\text{H}^+ + 4\text{e}^- \rightarrow 2\text{H}_2\text{O}$) at the cathode, and more water is transported from the anode to the cathode through the membrane via electro-osmotic drag [10–12]. The water at the cathode condenses and accumulates, blocking oxygen diffusion and causing a sudden decrease in the cell voltage. Simultaneously increasing the current density causes the membrane to dry out at the anode. The membrane is dehydrated by electro-osmotic drag from the anode to the cathode [13], in addition to the increased temperature from the electrochemical reaction and ohmic heat. The proton conductivity of the membrane is heavily dependent on its water content, meaning that dehydration of the membrane decreases proton conductivity, and thus, cell performance.

In a previous study, we achieved a performance of 0.55 V at 1.8 A cm⁻² without a significant voltage drop, even at a relatively high current density of over 1 A cm⁻², utilizing tightly aligned microcoils in the flow channel without a GDL. We have also measured the performance of conventional flow fields with GDLs; the performance showed a severe voltage drop starting at a relatively low current density of 0.6 A cm⁻² [14]. In general, GDLs work by distributing the gas from the flow channel to the land underneath in a conventional flow field [15]; however, when the GDLs and channel/land structure are combined, the water cannot be removed from underneath; this water accumulation results in a non-uniform blockage of gas supply to the catalyst layer, the well-known phenomenon of electrode flooding, which significantly decreases fuel-cell performance along with an accompanying increase in current density [16]. We have concluded that the microcoil flow channel can supply the reactant gas uniformly to the catalyst layer (in this work, no sign of flooding is visible up to 1.8 A cm⁻² in the polarization curve). Nonetheless, the GDL-less microcoil flow channel shows a larger high-frequency resistance (HFR) than conventional flow fields with GDLs. Due to fewer contact points between the microcoils and microporous layer (MPL), electron conduction occurs in the in-plane direction of the MPL, which causes a larger HFR in the microcoils with higher contact and concentration resistance from the point-to-surface contact on the MPL.

There is little information published in the literature pertaining to electron resistance in GDL-less PEFC stacks. Seyfang et al. reported the performance of GDL-less stacks utilizing micro-patterned glassy carbon flow fields and a catalyst-coated membrane (CCM) [17]. They found that the GDL-less stack had a higher ohmic loss than the GDL-containing stack due to the reduction of electron travel pathways through the thin catalyst layer in the GDL-less case. They also evaluated the ohmic loss for several channel geometries to verify the electron path through the catalyst layer, obtaining a linear correlation between the channel width and HFR of the fuel cell. They used the catalyst layer as the electron conductor and collector; however, problems with high ohmic loss and low gas diffusion were experienced directly under the land of the bipolar plate, especially at the cathode.

Other than the larger HFR for microcoil flow channels in GDL-less stacks, the high cost of microcoils must also be considered, especially if being mass-produced. Furthermore, tightly setting a number of microcoils onto the bipolar plate is quite time consuming. Therefore, we have prepared a corrugated stainless-steel mesh as the gas-flow channel with the expectation that the corrugated mesh may play a similar role as microcoil flow channels in order to reduce flooding. Here, we report the preparation, performance, and HFR of a corrugated mesh applied to GDL-less fuel cells, and the effect of MPL conductivity on the HFR using the equivalent circuit model to extract the MPL contribution for the HFR.

2. Experimental

2.1. Preparation of a corrugated mesh flow channel

The corrugated mesh flow channel was prepared with a stainless-steel mesh and corrugating roll. The stainless-steel mesh (nets101 Co., Ltd, Shimizu, Japan) was a twill weave-type SS316L material of 300-mesh with a fiber diameter of 50 μm. The cross-section shape of the corrugated mesh was triangular with a height of 0.3 mm and length of 0.3 mm. To corrugate the mesh, a customized corrugating roll was fabricated (MIKI SEISAKUSYO CO. LTD., Osaka, Japan) as shown in Fig. 1. The template grooves were first machined on the surface of the roll along the direction of the circumference, the plain mesh was inserted between the two rolls, and the fluted shape was finally transferred to the mesh under a certain compression pressure. Fig. 2 shows an optical microscope image of a cross-section of the corrugated mesh. Two different flow-channel patterns were formed in the gas-flow direction, namely a straight pattern (straight corrugated mesh) and meandering pattern (meandering corrugated mesh). The straight corrugated mesh had a high electrical resistance on both sides; therefore, the meandering corrugated mesh was made as a solution as described in Section 3.2. The meandering pattern adopted the shape of a sine curve with a length of 0.6 mm and amplitude of 0.2 mm in the same triangular cross-section using a similar corrugating roll template method.

2.2. Preparation of MPLs

MPLs were used in the anode and cathode catalyst layers to control fuel-cell water management [18]. Generally, the MPL is coated on the GDL; however, in the present study of GDL-less fuel cells, a free-standing MPL was required for use between the catalyst layers and corrugated mesh flow channels. The electron-conducting pathway from the catalyst to the bipolar plate in the present fuel cells is thought to be different from conventional fuel cells that utilize GDLs. The electron is first transferred vertically to the MPL and then moved horizontally within the MPL to the corrugated mesh contact point. To observe this effect, four different MPLs were fabricated having different conductivities using four

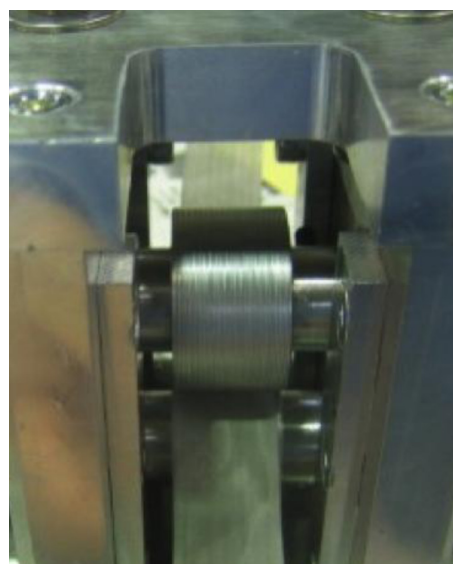


Fig. 1. Image of the roll corrugator used for production of corrugated mesh.

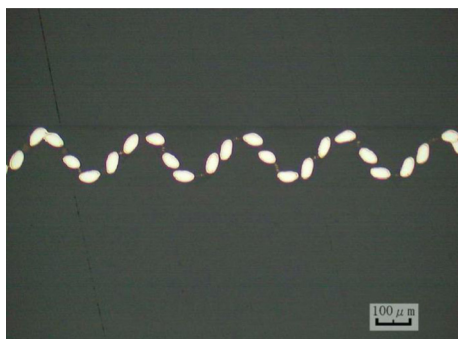


Fig. 2. Optical microscopic image of a cross section of the corrugated mesh.

different materials, and the in-plane and through-plane conductivities of these MPLs were measured.

The four different MPLs prepared with varying conductivities used the following materials: powdered carbon black (CB; Denka Black, Denki Kagaku Kogyo K.K., Tokyo, Japan); powdered graphite flake (GF; BF-1AT; diameter: 9 μm ; thickness: 1 μm ; Chuetsu Graphite Works, Osaka, Japan); powdered silver flake (SF; Ag-XF301; diameter: 7 μm ; thickness: 1 μm ; Fukuda Metal, Kyoto, Japan), and; through-hole stainless-steel foil with gold plating (SS; Hirai Seimitsu Kogyo Co., Gifu, Japan). The four MPLs were prepared as follows: 1) CB-MPL: CB, a polytetrafluoroethylene (PTFE) aqueous dispersion (D-1, Daikin Industries Ltd., Osaka, Japan), nonionic surfactant (Triton X-100, Sigma–Aldrich), and DI water were mixed with zirconia beads (1 mm) in a bead mill for 3 h at 400 rpm with a weight ratio of CB:PTFE:surfactant:water = 5:1:20:20. This solution was used to impregnate an expanded PTFE porous sheet (30 μm thickness, Poreflon Membrane, Sumitomo Electric Industries Ltd., Osaka, Japan), which was then dried at 350 $^{\circ}\text{C}$ for 60 min. 2) GF-MPL: GF, a PTFE aqueous dispersion, and ethanol with a weight ratio of GF:PTFE:ethanol = 5:1:5 were mixed, and the resulting paste was hot-pressed at 350 $^{\circ}\text{C}$ and 3 MPa for 10 min with a 40 μm -thick stainless-steel shim to control the compression thickness. 3) SF-MPL: SF, a PTFE aqueous dispersion, and ethanol with a weight ratio of SF:PTFE:ethanol = 5:1:5 were mixed, and the resulting paste was hot-pressed at 350 $^{\circ}\text{C}$ and 3 MPa for 10 min with a 40 μm -thick stainless-steel shim to control the compression thickness. 4) SS-MPL: a stainless-steel foil of 40 μm thickness was chemically etched to make through-holes having 30 μm diameters for the gas supply to reach the catalyst layer, which was then electroplated with 1 μm -thick gold as reported by F.-Y. Zhang [19]. Here, an expanded PTFE membrane was used for the CB-MPL to maintain sufficient strength for handling; because CB is nanosized with a spherical shape, the CB-MPL without the expanded PTFE was too brittle to handle during fuel-cell assembly. In contrast, GF and SF materials were micron-sized and plate-shaped such that the flakes were well aligned after hot-pressing, and were not too brittle to use in the subsequent evaluations.

2.3. Preparation of fuel cell

The bipolar plates for the fuel cell used in this study had 5 cm^2 active areas (1 $\text{cm} \times 5 \text{ cm}$) made of graphite (Mechanical Carbon Industry, Kanagawa, Japan). The end plates for these bipolar plates were made with stainless steel with eight holes for fastening; the fabricated plates were made to withstand a compression pressure of 1 MPa for fuel-cell assembly. The end plates had sheet heaters on the outside of the anode and cathode to control the cell temperature. A stainless-steel current collector with a 1 μm -thick gold plating was inserted between the bipolar plate and end plate on

both sides. Ethylene–propylene diene monomer (EPDM) rubber gaskets (0.6 mm thick, NOK Co., Tokyo, Japan) were used to surround the active area and seal the reactant gases. Bolt torques of 0.3 N m were used to achieve a compression pressure of 1.0 MPa for fuel-cell assembly.

Nafion (25 μm thick, NRE211, du Pont de Nemours, Delaware, USA) was chosen as the polymer electrolyte membrane, and carbon-supported platinum (Pt/C, 50 wt% Pt, TEC10E50E, Tanaka K.K., Tokyo, Japan) was selected as the catalyst. The catalyst-coated membrane (CCM) was prepared as follows: Pt/C powder was mixed with a Nafion dispersion (DE2020, du Pont de Nemours, Delaware, USA) using a zirconia bead mill (1 mm diameter beads) for 8 h on a rotation table (400 rpm speed). The catalyst solid contents were prepared using a 1:1 mixture of carbon support and Nafion ionomer. The catalyst was coated on both sides of the membrane with a spray coater (Mic Lab, Kanagawa, Japan) several times until achieving a coating thickness of about 30 μm . The platinum loadings were 0.4 mg cm^{-2} for both the anode and cathode. The coated membrane was dried at 80 $^{\circ}\text{C}$ for 60 min and annealed at 130 $^{\circ}\text{C}$ for 10 min to obtain the CCM. The CCM was hot-pressed with MPLs on both sides of the anode and cathode at 130 $^{\circ}\text{C}$ and 3 MPa g for 10 min using 200 μm -thick Teflon backing sheets on both sides to avoid MPL attachment to the hand-press plates.

Four flow-channel designs were assessed in this study as shown in Fig. 3(a)–(d) and Table 1. The first design was a conventional flow field with a 50 mm-long and 1 mm-wide cathode land, and a cathode with channel dimensions of 50 mm length, 1 mm width, and 1 mm depth. The GDL was laid between the flow field and CCM with CB-MPL (Design 1). The second design utilized a straight corrugated mesh on just the cathode, which was laid on a pool-shaped graphite bipolar plate that directly covered the CCM with CB-MPL. The anode was the conventional flow field with a GDL (Design 2). The third design utilized a straight corrugated mesh for both the anode and cathode with CB-MPL (Design 3). The fourth design utilized a waved corrugated mesh for the anode and straight corrugated mesh for the cathode with CB-MPL (Design 4).

Furthermore, for Design 4, the effect of MPL conductivity against fuel-cell performance and HFR was evaluated with four different MPLs, namely Design 4a: CB-MPL, Design 4b: GF-MPL, Design 4c: SF-MPL and Design 4d: SS-MPL. Fig. 2 shows a scheme of the evaluated flow channels, and Tables 1 and 2 show the configurations of the corresponding fuel cells.

2.4. Characterization of fuel-cell performance and HFR

The single cell was mounted on a fuel-cell test stand (Chino Co., Tokyo, Japan) equipped with mass flow controllers, an electronic loading device (Kikusui Electronics Co., Yokohama, Japan) for controlling the electric current, an AC milliohm tester (Model 3566, Tsuruga Electric Co., Osaka, Japan) with a constant HFR of 1 kHz, and a computer for equipment monitoring and data collection.

Gas flows for the anode and cathode were held constant to measure the polarization curves; 0.47 L min^{-1} of pure hydrogen was supplied to the anode (stoichiometry ratio SR_a : 9.0 at 1.5 A cm^{-2}), and 1.1 L min^{-1} of air was supplied to the cathode (stoichiometry ratio SR_c : 9.0 at 1.5 A cm^{-2}). The reactants were supplied with a counter flow as well. All reaction gases were humidified to 100% relative humidity (RH) with temperature-controlled water bubbling tanks. The fuel-cell temperature was maintained at 70 $^{\circ}\text{C}$ with a heater, and thermocouples were inserted into the cathode bipolar plate. As for the orientation of those fuel cells, the membrane-electrode assemblies (MEAs) were located vertically and the flow channels were set horizontally; consequently, gravity did not assist in the removal of liquid water from the channel.

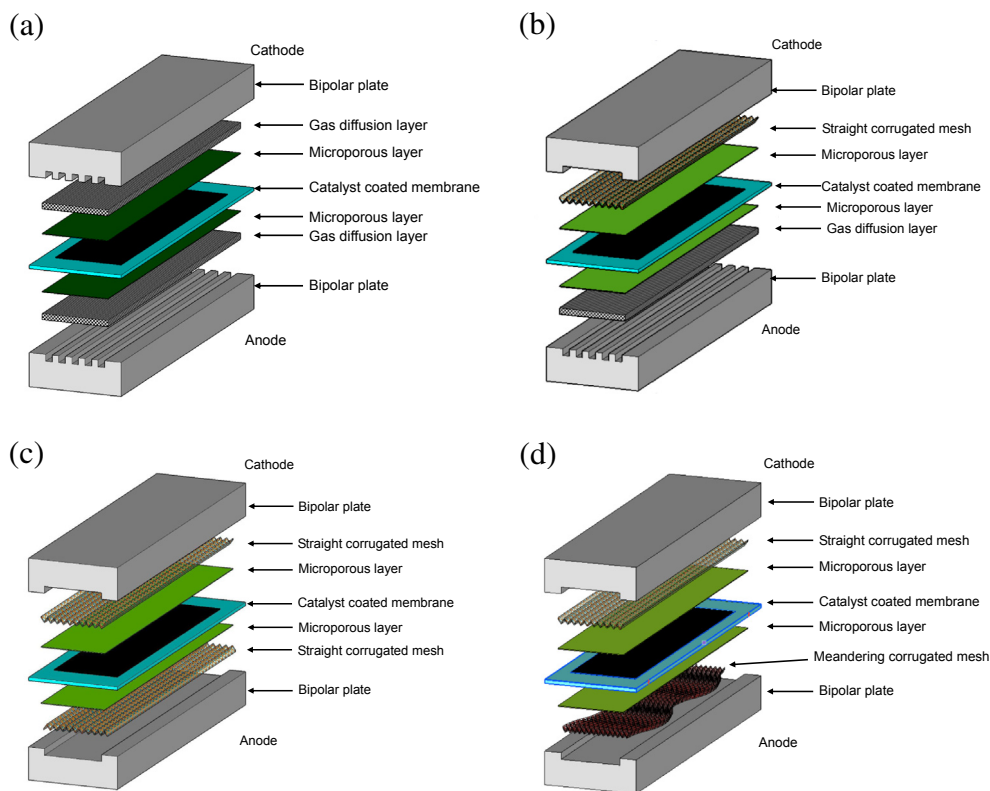


Fig. 3. Schematic image of (a) Design 1: conventional flow field with GDL, (b) Design 2: straight corrugated-mesh flow field for cathode, (c) Design 3: straight corrugated mesh flow field for anode and cathode, and (d) Design 4: wavy corrugated mesh flow field for anode and straight corrugated mesh for cathode.

All power-generation processes were conducted under atmospheric conditions. All fuel-cell evaluations were conducted after 10 h of aging at a current density of 1.0 A cm^{-2} , temperature of 70°C , anode feed gas flow of 0.5 L min^{-1} with 100% humidified hydrogen, and cathode feed gas flow of 0.5 L min^{-1} with 100% humidified air.

The small-area cell and high stoichiometry employed was to obtain uniform distributions of the reactants, as the high stoichiometry conditions can help extrude accumulated water in the channel and reduce channel flooding such that the voltage loss caused by flow non-uniformity and oxygen depletion in the channel can be minimized. Siefert et al. investigated the voltage loss and voltage fluctuations for parallel straight flow channels having different stoichiometries and different aspect ratios of the same active area, where the water accumulates mainly in the flow channel, causing channel flooding [20]. They obtained a relatively low current density of 0.4 A cm^{-2} , which is well within the linear ohmic region of the polarization curve and is far from the non-linear mass transport-limited electrode region, where channel flooding is not present. Finally, they generalized the effects of channel plurality and stoichiometry on the normalized voltage loss

as $32 N \cdot A_c/A/\zeta$ and the standard deviation of voltage fluctuations as $34 N \cdot A_c/A/\zeta^2$, where A_c is the cross-sectional area of each channel, A is the active area, N is the number of channels, ζ is the stoichiometry and $N \cdot A_c/A$ is the ratio of the total channel cross-sectional area to the active area. These equations were applied to the present conventional system with a stoichiometry of 9.0 for the flow-channel dimensions and MEA materials described here, which are quite similar to Siefert's system. The present system exhibited a voltage loss of 3.6% and voltage fluctuation of 0.42%; thus, the conventional design described can minimize channel flooding.

Even at such a high stoichiometry, the electrode can be flooded as reported by Yamada et al. from their results of experimental and simulation studies [21]. They showed that electrode flooding starts at a current density of 0.5 A cm^{-2} , and that voltage drops significantly around 1.2 A cm^{-2} . Their simulations also showed that liquid-water saturation in the GDL reaches a value greater than 0.8, especially the region under the flow-field land.

The present work focuses on electrode flooding; thus, a high air flow rate of 1.1 L min^{-1} and equivalent stoichiometry of 9.0 at 1.5 A cm^{-2} was used for the cathode to minimize the channel flooding effects on voltage loss. A stoichiometry of 9.0 for a

Table 1
MEA and flow field configuration of each design.

	Flow field		GDL		MPL	
	Anode	Cathode	Anode	Cathode	Anode	Cathode
Design 1	Conventional	Conventional	TGP-H-090	TGP-H-090	CB	CB
Design 2	Conventional	Straight corrugated-mesh	TGP-H-090	None	CB	CB
Design 3	Straight corrugated-mesh	Straight corrugated-mesh	None	None	CB	CB
Design 4	Meandering corrugated-mesh	Straight corrugated-mesh	None	None	CB	CB

CB: carbon black.

Table 2
MPL materials and electron conductivities in Design 4.

	MPL material		MPL volume resistivity	
	Anode	Cathode	In-plane (Ω cm)	Through-plane (Ω cm)
Design 4a ^a	CB	CB	2.5×10	1.3×10
Design 4b	GF	GF	4.8	3.9
Design 4c	SF	SF	6.4×10^{-4}	1.9×10^{-4}
Design 4d	SS	SS	1.1×10^{-4}	7.3×10^{-5}

CB: carbon black, GF: graphite flake, SF: silver flake, SS: stainless steel.

^a Design 4a is same as Design 4 in Table 1.

conventional parallel flow channel is generally sufficient to avoid substantial effects attributed to channel flooding. However, for the corrugated mesh flow channel, the effects of channel flooding and electrode flooding were not separated because of differences in the wettability of the carbon flow field and gold-plated stainless-steel corrugated mesh, the air average velocity of each flow field, and the electrode interface and gas flow in the conventional flow field with the GDL and in the corrugated mesh with the MPL. Thus, the equations described above could not be applied in this regard to estimate the effects of channel flooding owing to their limitations in describing geometry and materials. Nonetheless, the same operation condition was used for the corrugated mesh flow field as for the conventional channel to compare these polarization curves to assess its advantages and disadvantages.

2.5. In-plane and through-plane electronic conductivity of MPLs

For the present fuel cells, the electron-conducting pathway from the catalyst layer to the bipolar plate is thought to be different from conventional fuel cells, and thus is expected to provide different HFRs. For example, an electron in Design 1 is transferred from the catalyst layer through the MPL vertically to the GDL because the GDL uniformly covers the entire active area. In Designs 2–4 without GDLs, electrons in the catalyst layer are first transferred vertically to the MPL and then move horizontally within the MPL to the contact point of the corrugated mesh. To characterize this, the electronic conductivity of MPL in the in-plane and through-plane directions was measured.

The in-plane conductivity was measured at 25 °C following the standard ASTM C611 method, using four-point detectors in a direct current [22]. Sample strips (0.5 cm \times 4.0 cm) of the MPL and GDL were used. Resistances obtained with a resistance meter (1750 LCR Dig-Bridge with Kelvin clip leads, Quad Tech Inc., Maynard, USA) were converted to conductivity using the sample geometries.

The measurement of through-plane conductivity was performed at 25 °C in accordance with the method described in Ref. [23]. A 20 mm round sample in diameter was placed on a load cell (ElectroPuls™ E1000, Instron, Massachusetts, USA) between two gold-plated pedestals, and the sample was subjected to a compression pressure of 1 MPa. The same resistance meter as described above in this section was used to obtain the resistance of the sample. After the compression stress was stabilized (30–60 min), the resistance was measured and converted to conductivity using the sample geometry.

3. Results and discussion

3.1. Polarization curves

Fig. 4 shows the polarization curves for Design 1 (conventional flow field), Design 2 (straight corrugated mesh on cathode), Design 3 (straight corrugated mesh on anode and cathode) and Design 4 (meandered corrugated mesh on anode and straight corrugated

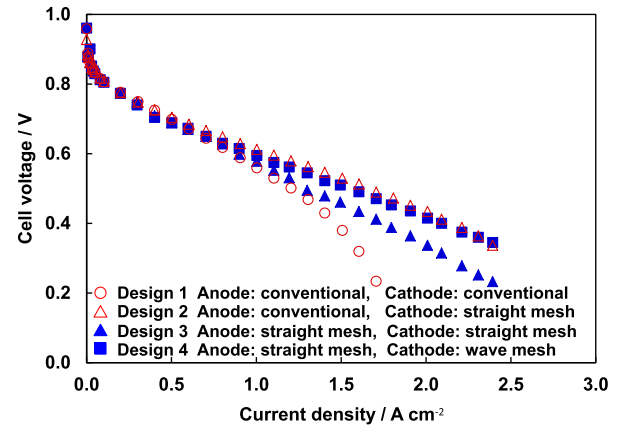


Fig. 4. Polarization curves for the conventional flow field with a GDL and the corrugated mesh flow field without a GDL (Design 1–4), obtained under $RH_{\text{anode}} = 100\%$, $RH_{\text{cathode}} = 100\%$, ambient pressure at the outlets, cell temperature = 70 °C, and hydrogen and air supplied in constant flow ratio of 0.47 L min⁻¹ and 1.1 L min⁻¹, respectively.

mesh on cathode) as described in Table 1. Fig. 5 shows the HFR for Designs 1–4 at 1 kHz, and Fig. 6 shows the IR-corrected polarization curves for all four designs. The IR corrections were performed to compensate for the ohmic loss for each design using HFR; Fig. 6 shows both the activation loss and mass-transfer loss (flooding) [24].

As seen in Fig. 6, all four IR-corrected polarization curves are nearly the same for the lowest current density up to 0.3 A cm⁻². This observation indicates that the activation loss for each design is the same, that the gas is equally supplied to the catalyst in each design, and that the CCMs and MPLs have similar properties. In addition, the HFR may represent the ohmic resistance even though the electron pathways are different for Design 1 and Designs 2–4 as indicated by the similar IR-corrected polarization curves. For Design 1, the cell voltage gradually decreases due to flooding as the current density exceeds 0.5 A cm⁻² (Fig. 6) with a rapid voltage drop down to 0.3 V at 1.7 A cm⁻². In contrast, Designs 2–4 utilizing corrugated mesh exhibit performances without significant voltage drops caused by electrode flooding.

Hussaini and Wang have recently characterized water and air permeabilities of GDLs [25], showing that the air relative permeability decreases rapidly with increasing water saturation. The gas can travel through the GDL through a capillary fingering network of liquid water [26]. Presently, it is not certain whether water saturation occurred during the operation of Designs 1–4, but according

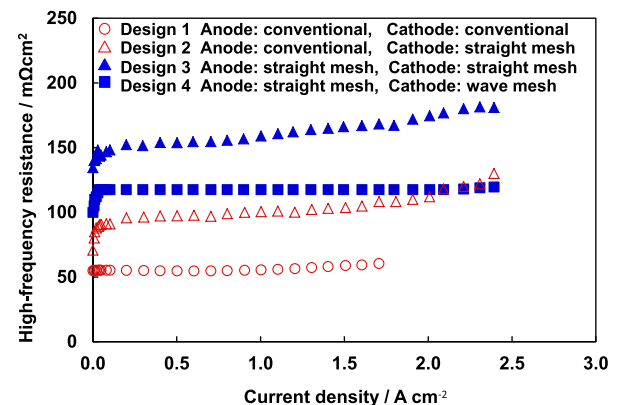


Fig. 5. High-frequency resistance (HFR) for Designs 1–4.

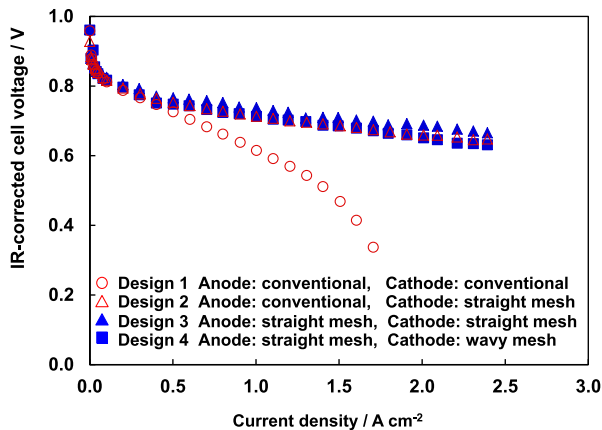


Fig. 6. IR-corrected polarization curves for Designs 1–4.

to the rough estimation of temperature in the GDL described in a previous work [14], the temperatures of the GDL and MPL could be estimated as 82–83 °C against an operation temperature of 80 °C. Thus, these temperatures indicate that liquid water might be present in the GDL and MPL. Designs 2–4 exhibit performances with both reduced flooding and voltage drops, even in the presence of liquid water. These performances have been discussed in our previous work [14]; it is suggested that microcoils provide a uniform gas supply onto the catalyst layer, even in the presence of liquid water, and that flooding occurs only for a specific combination of land/channel structure and GDL, where the liquid water accumulates under the land regions of the cathode. In Designs 2–4, the corrugated mesh appears to supply the gas uniformly to the active area in a similar fashion as the microcoils.

In addition to providing a uniform gas supply with the corrugated mesh, the GDL-less design efficiently supplies gas to the catalyst layer. Specifically, the water on the top surface of the MPL can be easily removed by dynamic gas flow through the corrugated mesh and thus, the amount of liquid water in the MPL is kept at a sufficiently low saturation level to allow wider gas diffusion. Furthermore, because the diffusion length in the MPL is smaller than in the GDL and MPL, the gas diffuses noticeably faster in the GDL-less designs than the conventional design with GDL. In addition, a comparison of Designs 2 and 3 reveals that only the cathode flow field exhibits an effect on electrode flooding, as the three designs with corrugated mesh on the cathode display similar behaviors (Fig. 6), regardless of the conventional flow field or corrugated mesh flow channel utilized on the anode.

Fortunately, the high stoichiometry used (9.0) could minimize the effect of channel flooding, even with the hydrophilic and rough surface of the corrugated mesh flow channels. As reported by Lu et al., channel surface wettability can strongly affect channel flooding [27]. The researchers observed two phase flows in a flow channel of 0.7 mm width and 0.4 mm depth on uncoated, hydrophilic-, and hydrophobic-coated Lexan plates. They found that at a high liquid-water flow, which is equivalent to a current density of 1.0 A cm⁻², the hydrophilic channel shows a greater flow fluctuation than that of the uncoated and hydrophobic channels; this is thought to be because water can wick into the channel corners and is removed through continuous film flow at a higher rate than that driven by the air flow. In addition, water tends to adhere to the channel wall with high surface tension instead of being removed by air shearing. Furthermore, they also found that the flow fluctuation decreases as air velocity increases, and that flow fluctuation becomes less than 50% at a flow velocity of 5 m s⁻¹ in their case. In the present case utilizing the corrugated mesh flow channel, the metal

mesh is most likely hydrophilic and rough, and the cross-section dimension of the corrugated mesh is 0.3 mm wide and 0.3 mm deep. The water probably tends to be present as a continuous film on the corrugated mesh surface. However, the average gas velocity at this flow rate is observed to be 6.7 m s⁻¹, which seems to be a high enough value for uniform distribution in the corrugated mesh channel of the cathode (Fig. 6). Therefore, channel flooding might not have a strong effect on the performances of Designs 2–4.

The through-plane water transport from the electrode to the channel can also be strongly influenced by surface wettability of the channels. The metal mesh can be hydrophilic while the GDL is hydrophobic; thus, the behavior of the liquid water from the MPL to the corrugated mesh and GDL should be different with different surface wettabilities. Consequently, this may alter the liquid water behavior, which can impact current density. Turhan et al. investigated the effects of channel-wall wettability of gold-plated and PTFE-coated flow channels using neutron radiography to detect the liquid water in the channel, GDL, MPL, and catalyst layer in the fuel cell [28]. They suggested that the hydrophilic interface enhances capillary suction from the GDL, as does the hydrophilic wall in the form of film flow, and results in less water storage in the GDL and MPL. Another study by Wang describes fuel-cell performance as a function of wettability of an entirely hydrophilic GDL and super-hydrophobic/hydrophilic/super-hydrophobic GDL sandwich [29]. The hydrophilic GDL lowers the performance because the liquid water could quickly distribute in the GDL; however, the droplet resists being detached from the GDL surface by air shearing due to the high surface tension, resulting in a reduced gas permeability as a consequence of this thin water film.

These two cases indicate that the hydrophilic wall of flow channel or the hydrophilic GDL can pull the liquid water from the next layer by capillary force and that the liquid water tends to form a thin film on the air-flow interface of the flow channel and the GDL. If the air-flow velocity is not sufficiently high to remove the liquid water on the hydrophilic surface, the water can flood the channel or GDL surface. In the present case, the hydrophilic metal mesh channel on the MPL may enhance liquid-water transport from the MPL to the channel, allowing a water film to be formed on the metal mesh. With respect to channel flooding, a high stoichiometry could help to remove the water as described in a previous paragraph in this section. Furthermore, unlike the case of the hydrophilic GDL, the present system utilizes a hydrophobic MPL at the air interface; thus, a water film could not form on the hydrophobic MPL surface, and gas could likely be supplied into the MPL without liquid water blocking the process. Further studies are required for this fuel cell in terms of complete characterization and investigation of the effects of corrugated mesh on the MPL and operation conditions, as well for more detailed and accurate mechanistic studies of water transport.

Although Designs 2–4 exhibit less flooding, their performances are slightly different because of the different HFR values for these designs along with varying flow channel patterns on the anode and cathode; HFR performances are discussed in the next section (Section 3.2).

3.2. Effect of flow-channel pattern on high-frequency resistance (HFR)

Fig. 5 shows the HFR for Designs 1–4. Design 1 utilizes the conventional flow field, and GDLs on both the anode and cathode exhibit an HFR of 55–60 mΩ cm², in agreement with the values published in the literature (50–70 mΩ cm²) [30–32]. Design 2, which uses a corrugated mesh directly on the MPL on the cathode, has an HFR of 90 mΩ cm², and Designs 3 and 4, which use corrugated mesh at both the anode and cathode, have HFR values of

150 mΩ cm² and 120 mΩ cm² respectively. These GDL-less designs (Designs 2–4) exhibit a relatively higher HFR than that of conventional Design 1. As discussed in a previous work [14], these results indicate that the electron pathways for these designs are different. In Design 1, the pathway could be vertical from the MPL/catalyst layer to the GDL because the GDL makes surface-to-surface contact with the entire MPL. However, in Designs 2–4, the pathway could be the combination of both vertical and horizontal directions: vertical from the catalyst layer to the MPL and horizontal from the MPL to the contact point of the corrugated mesh. This is because the corrugated mesh does not cover the entire active area and can make line-to-surface contact with the MPL. The corrugated mesh has contacts on the MPL at intervals in the corrugation cycle, meaning that the corrugated mesh has fewer contact points with the MPL. The corrugation peak line is made of a number of twill-woven fibers, and the contact line is the aggregate of contact points. In this paper, the term “line” is used for the aggregate contact points of the fibers.

Let the resistance of CCM be R_{CCM} , the resistance of GDL/MPL be R_{GDL} , and the resistance of corrugated mesh/MPL be R_{mesh} . The overall resistance for Design 1 is described as follows:

$$R_{\text{GDL}} + R_{\text{CCM}} + R_{\text{GDL}} = 55 \text{ m}\Omega \text{ cm}^2 \quad (1)$$

The overall resistance for Design 2 is described as:

$$R_{\text{GDL}} + R_{\text{CCM}} + R_{\text{mesh}} = 90 \text{ m}\Omega \text{ cm}^2 \quad (2)$$

These overall resistances contain the material and contact resistance in the designs along with the electron pathway. From Eqs. (1) and (2), the overall resistance for Design 3 should be:

$$R_{\text{mesh}} + R_{\text{CCM}} + R_{\text{mesh}} = 125 \text{ m}\Omega \text{ cm}^2 \quad (3)$$

However, Fig. 5 shows that the HFR for Design 3 is 150 mΩ cm², which is bigger than the estimated value of 125 mΩ cm² as determined from Eq. (3). This indicates that another factor might affect the experimental resistance, creating a higher HFR than expected.

Design 3 utilizes the straight pattern as the flow channel on corrugated meshes (straight corrugated mesh) for the anode and cathode as shown in Fig. 3(c). In this case, the corrugation line of the straight pattern on both sides of the MPL/CCM/MPL might not meet at the same contact line because of engineering and alignment tolerances. These unaligned line-to-line sandwiches should reduce the vertical compressive contact pressure and increase the shear stress between the MPL and corrugated mesh. In Design 3, this low-contact pressure increases the contact resistance between the interfaces and HFR. On the other hand, the corrugated mesh and GDL in Design 2 could make line-to-surface sandwiches, and the contact point could experience a vertical contact pressure, resulting in a better contact between the MPL and corrugated mesh even with these tolerances.

A meandering pattern as a flow channel was fabricated on corrugated meshes with the same triangular cross-section (meandering corrugated mesh) as described in Section 2.1. The meandering corrugated mesh was laid on the anode and the straight corrugated mesh was laid on the cathode (Design 4) as shown in Fig. 3(d). Utilizing the meandering flow channel at the anode is a reasonable arrangement because the anode needs a low flow rate and hydrogen has a low viscosity; accordingly, the pressure drop at the anode should be even lower with a tortuous flow channel. However, these pressure-drop requirements are dependent on the application for which the fuel cell is fabricated.

In Design 4, the straight corrugation line at the anode and the meandering corrugation line at the cathode must meet to make crossline sandwiches through the MPL/CCM/MPL. As seen in Fig. 5,

Design 4 has a lower HFR than Design 3, indicating that the crossline-to-crossline sandwiches could make better contacts with increased compressive pressure on the MPL. The HFR value of 120 mΩ cm² for Design 4 roughly agrees with the estimated value of 125 mΩ cm² as determined by Eq. (3).

Although Eq. (3) could be generated from Eqs. (1) and (2), Eq. (1) is based on the surface-to-surface sandwich of Design 1, while Eq. (2) is based on the surface-to-line sandwich. Therefore, Eq. (3) should not be able to explain the crossline sandwich precisely. The overall resistances R_{mesh} , R_{GDL} , and R_{CCM} in Eqs. (1)–(3) contain contact resistance, but the contact resistance should differ in the sandwich configurations. To estimate the HFR for each design, including the effects of contact pressure and contact resistance as well as conductivities of the materials, current efforts in our lab are being dedicated to simulating the resistance via a 3D finite element model (FEM) and will be reported elsewhere.

Even with the superior contact in Design 4, the HFR is still higher than in Design 1. As described previously, the higher HFR should be derived from the longer electron-pathway running horizontally through the MPL. Therefore, we next evaluated several MPLs with different conductivities in Design 4, which are described in Section 3.3.

3.3. Effect of MPL conductivity on high-frequency resistance (HFR)

Using Design 4, the effect of MPL conductivity on the HFR was evaluated utilizing the meandering corrugated mesh at the anode and the straight corrugated mesh at the cathode. Design 4 utilizes CB-MPL and will be denoted as Design 4a, GF-MPL as Design 4b, SF-MPL as Design 4c, and SS-MPL as Design 4d. Table 2 shows the MPL material for each design and the in-plane and through-plane volume resistivity (conductivity^{−1}) for each MPL. There was some concern that silver might not be durable enough for extended use in the fuel cell; a silver-flake MPL was used in evaluations on the basis of the results described by Ge et al., who used a silver mesh as the cathode GDL for cathode catalyst layer observations in their work [33]. Their results did not seem to suffer from silver corrosion in the short-term evaluation. It should be noted that silver is not the final material, and another durable and conductive material must be identified for use in MPLs in the future.

Fig. 6 shows the polarization curves for Designs 4a–d. Figs. 7 and 8 show the HFR and IR-corrected polarization curves, respectively, for Designs 4a–d. As seen in Fig. 8, all four IR-corrected polarization curves are nearly the same for the lowest current density up to 0.3 A cm^{−2}; these observations indicate that the activation loss for each design is the same, that the gas is equally supplied to the catalyst in each design, and that the CCMs and MPLs have similar properties.

As shown in Fig. 9, Designs 4b and 4c have a similar behavior up to a current density of 3.0 A cm^{−2} without significant flooding, even when utilizing different MPL materials and shapes. Although the MPLs in Designs 4b and 4c were made with flake powders in a layered structure, these flake-powder MPLs are shown to supply enough gas, even with a diffusion pathway differing from that for the carbon black MPL in Design 4a, at least under a high stoichiometry (9.0) at 1.5 A cm^{−2} with a fully humidified anode and cathode gas supply. Certainly the performances for Designs 4b and 4c show less flooding, but such a high stoichiometry is not practical to assess the advantages of each MPL prepared with different materials and possessing different pore structures, especially for flooding evaluations.

To the best of our knowledge, no research paper has been published describing the effects of flake-shaped MPL particles on fuel-cell performances. Many papers, however, have reported that gas diffusivity in the MPL is based on porosity, pore-size, and

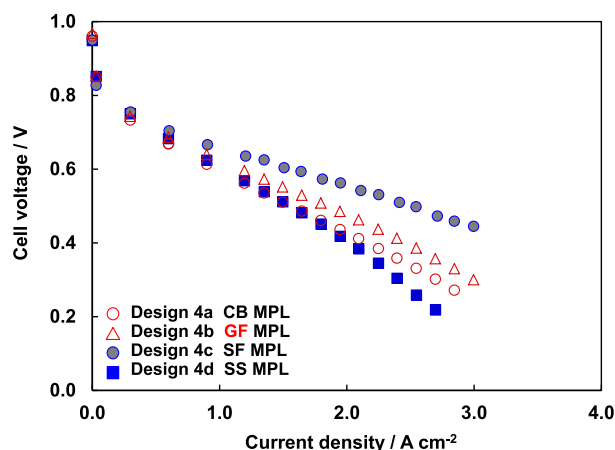


Fig. 7. Polarization curves for Design 4 with four different MPL (Designs 4a–d), obtained under $RH_{\text{anode}} = 100\%$, $RH_{\text{cathode}} = 100\%$, ambient pressure at the outlets, cell temperature = 70°C , and hydrogen and air supplied at a constant flow ratio of 0.47 L min^{-1} and 1.1 L min^{-1} , respectively.

tortuosity; furthermore, connectivity, hydrophobicity, and thermal/electrical conductivity in combination with the above three properties can result in differing liquid-water saturation, distribution, and morphology formed by capillary and temperature-driven flows in the GDL and MPL. Moreover, changes in liquid-water surface film formation, which can reduce gas diffusivity and cause cathodic flooding, can also result from changes in these material characteristics [34–37]. Finally, these MPL properties may also affect the net water transport across the membrane, which can cause membrane dry-out or GDL flooding [38,39]. Specifically, as reported by Morgan et al. [39], the particle size (5, 17, and $55\text{ }\mu\text{m}$) of MPLs can affect fuel-cell performance; the researchers found the performance of a $17\text{ }\mu\text{m}$ particle to be superior among the three particles tested in terms of balancing membrane dry-out and GDL flooding under dry and wet conditions. This result suggests that a particle size in the micron range should be carefully considered with respect to fuel-cell performance, especially for limitations in current density mainly determined by flooding behaviors. In the present case, the flow-field structure without a GDL is quite different, and the flake-shaped MPL particle can form different layered pore structures. Thus, the conclusions of Morgan et al. cannot simply be applied for the present case. The GF particle has a diameter of $9\text{ }\mu\text{m}$ and thickness of $1\text{ }\mu\text{m}$, and SF has a diameter of $9\text{ }\mu\text{m}$ and thickness of $1\text{ }\mu\text{m}$; these materials are therefore likely to form similar pore

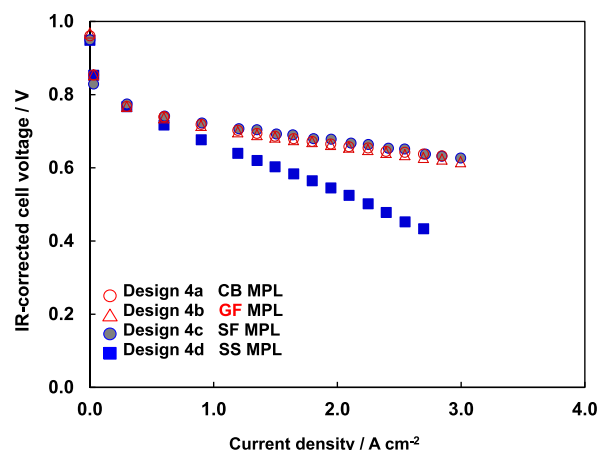


Fig. 9. IR-corrected polarization curves for Designs 4a–d.

structure in the MPL. In addition, both of the MPLs have the same PTFE content, suggesting that the hydrophobicity of these MPLs is probably similar. Therefore, water transport by the capillary-driven flow through GF-MPL and SF-MPL in the present fuel-cell operation is thought to be similar and the flooding behavior in the fuel cell utilizing those MPLs in Fig. 6 is also thought to be similar so that the differences in these performances might derive dominantly from the electron resistance of the MPLs, as will be discussed later in this section.

It is important to note that even if the capillary-driven water flow in these MPLs may be similar, their thermal and electric conductivities, overall heat transfer, and ohmic heat generation are different; thus, these properties can generate different temperature distributions and provide different temperature-driven water flows, which can give rise to different flooding behaviors in the fuel cells. The advantages of flooding control in the flake-shaped and nano-sized particles in the MPLs were not assessed because of the lack of mass-transport properties of the flake-shaped particle; further studies are therefore required for the characterization and investigation of structural and material effects of the MPL components. In addition, an examination of varying operating conditions on these fuel cells is required, especially for those with moderate air stoichiometry.

Fig. 10 shows a polarization curve and HFR for a lower stoichiometry of 3 for Design 4c using SF-MPL as an examination of performance under practical operation conditions. Constant flow rates of 0.16 and 0.37 L min^{-1} were employed at the anode and cathode,

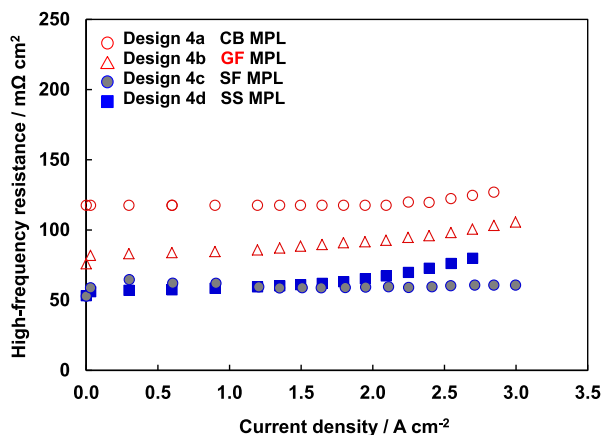


Fig. 8. High-frequency resistance (HFR) for Designs 4a–d.

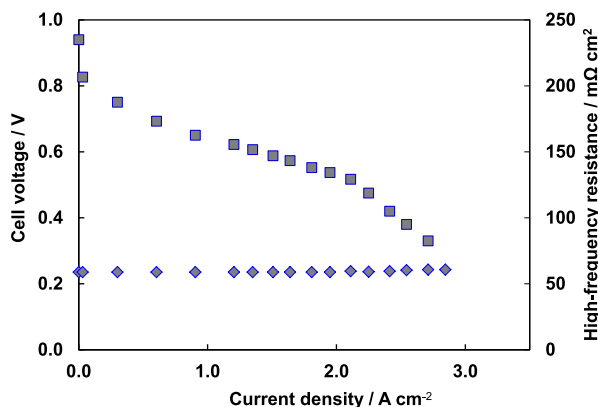


Fig. 10. Polarization curve and HFR for Design 4c under a stoichiometry of 3.0.

respectively, during the operation, which is equivalent to a stoichiometry of 3.0 at 1.5 A cm^{-2} . Other operation conditions were set the same as that indicated in Fig. 7. As shown in Fig. 10, the HFR is similar as that for a stoichiometry of 9.0 (Fig. 8). The performance begins to drop at a current density of about 2.0 A cm^{-2} , suggesting that flooding could affect mass transfer somewhere in the fuel cell; however, it is unclear from the one polarization curve exactly where the flooding occurs. It is suggested that the lower average air velocity in the cathode channel (2.3 m s^{-1}) might not be able to remove water from the surface of the corrugated mesh or the MPL, which would cause channel flooding. Further study is also required for a better understanding of the effects of stoichiometry dependency. In contrast to Design 4c, Design 4d shows flooding. This might be caused by the decreased diffusivity of the SS-MPL, where the reactant gas could not diffuse in the in-plane direction, but instead might diffuse in the catalyst layer from the through-holes. In addition, the flooding performance might be caused by the facile accumulation of water on the hydrophilic surface of the gold-plated layer on the SS-MPL [19].

As shown in Fig. 8, the HFR for Designs 4a–d are 120, 85, 65, and $57 \text{ m}\Omega \text{ cm}^2$, respectively. The HFR order of Design 4d < Design 4c < Design 4b < Design 4a mimics the conductivity of the MPL where $\text{SS} < \text{SF} < \text{GF} < \text{CB}$. Therefore, the MPL conductivity appears to have an effect on the HFR for each design. A frequency of 1 kHz was applied with an AC milliohm tester in the HFR measurement, which could detect the ohmic resistance of the electrolyte membrane, catalyst layer, MPL, and external parts (corrugated mesh, end plate, current collector, and wire/connector) as well as the contact resistance between each layer interface [40–42]. The resistance of these external parts can be neglected because they are made of gold-plated metal. Furthermore, the resistance of the electrolyte membrane and catalyst layer should be the same for each design, especially at the lower current density, because each design utilizes the same membrane and catalyst layers and operates under fully humidified conditions [43]. Therefore, the HFR difference between each design is derived from the conductivity differences of the MPLs.

An equivalent electrical circuit model was created to calculate the MPL resistance contribution of the HFR for each design. As shown in Fig. 11, the two-dimensional model with in-plane and through-plane resistance represents the electron resistance in the MPL from the catalyst layer to the contact point of the corrugated mesh on the MPL. The combined resistance is calculated in this circuit model under the following assumptions:

1. The MPLs at the anode and cathode have the same resistance. One side is considered in the model and the resistance is doubled for both sides.
2. The half pitch of the contact point of the corrugated mesh is considered symmetrical.
3. The catalyst layer has the same potential throughout the layer.
4. The MPL has anisotropic conductivity for the in-plane and through-plane directions.
5. The contact resistance between the catalyst layer and MPL and between the MPL and corrugated mesh can be ignored.
6. The in-plane electron conduction in the catalyst layer is also ignored.

As shown in Fig. 11(b), the model is divided into N units (Units 1 – N) and each unit has in-plane resistance R_0 and through-plane resistance R_1 . In Unit 1, the combined resistance R_{C1} is described as follows:

$$R_{C1} = \frac{1}{\frac{1}{R_0 + R_1} + \frac{1}{R_0}} \quad (4)$$

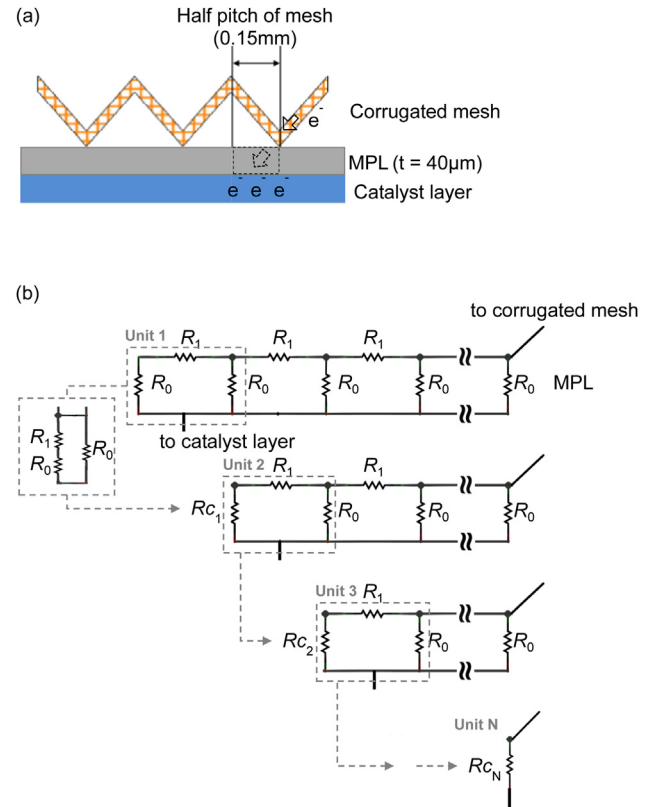


Fig. 11. Scheme of the catalyst layer, MPL, and corrugated mesh for electron conduction. (a) The sketch of the MPL, used for the construction of the continuous model. (b) The one-dimensional transmission line equivalent circuit for the MPL, where the elementary unit with through-plane electron resistivity R_0 and in-plane electron resistivity R_1 .

Then, in Units 1 and 2, the combined resistance R_{C2} is described with R_{C1} as follows:

$$R_{C2} = \frac{1}{\frac{1}{R_1 + R_1} + \frac{1}{R_0}} \quad (5)$$

Finally, in all Units 1 – N , the combined resistance R_{CN} is described with R_{C1} as follows:

$$R_{CN} = \frac{1}{\frac{1}{R_{N-1} + R_1} + \frac{1}{R_0}} \quad (6)$$

The conductivity of each MPL shown in Table 2 is used for the calculations with Eqs. (4)–(6), and the dimensional information (MPL thickness, contact-point interval, and active area) is also used to normalize the resistance to area resistivity (resistance per unit active area). Fig. 12 shows the plot of the estimated area resistivity of MPL for Designs 4a–d against the experimental HFR at 0.1 A cm^{-2} in the fuel-cell evaluation. The estimated MPL area resistivity and HFR appear to have a good correlation, where the MPL area resistivity linearly contributes to the total HFR in the fuel cell. Designs 4c (SF-MPL) and 4d (SS-MPL) have similar conductivities of 6.4×10^{-4} and $1.1 \times 10^{-4} \Omega \text{ cm}$, respectively, and similar estimated resistances of 6.0×10^{-4} and $2.2 \times 10^{-4} \text{ m}\Omega \text{ cm}^2$, respectively. Each design has different HFRs ($62 \text{ m}\Omega \text{ cm}^2$ and $55 \text{ m}\Omega \text{ cm}^2$, respectively) than would be expected from similar conductivities and estimated area resistivities.

As described in assumption 5 above, the contact resistance between the MPL and catalyst layer is ignored in this model, but SF-

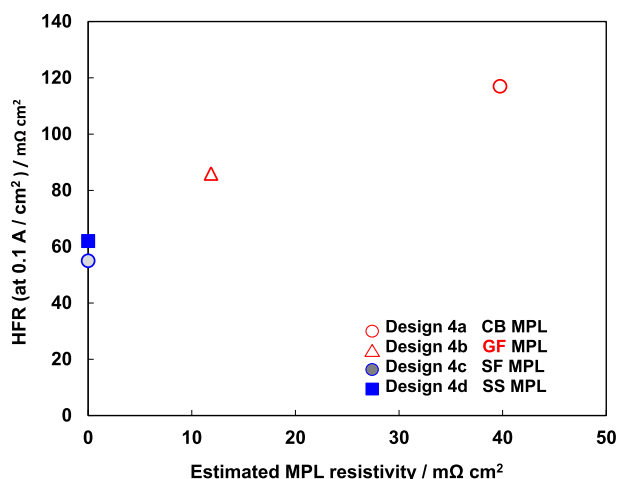


Fig. 12. A plot of the estimated area resistivity of MPL for Designs 4a–4d against the experimental HFR at 0.1 A cm⁻².

MPL and SS-MPL might have quite different contact resistances between the catalyst layer and MPL. The contact resistance is strongly dependent on the contact pressure [44]. In the present design, compression pressure is added onto the MPL from the corrugation line on the corrugated mesh, and the compression pressure is distributed via the MPL onto the catalyst layer. Generally, the uniformity of pressure distribution depends on the rigidity of the substrate [45]. SS-MPL, which is made of stainless-steel foil, is more rigid than SF-MPL, which is made of silver-flake powder bonded with PTFE. Thus, SS-MPL distributes the stacking pressure onto the catalyst layer more uniformly than SF-MPL, and SS-MPL makes better contact with the catalyst layer. Therefore, Design 4d utilizing SS-MPL has a lower contact resistance between the catalyst layer and MPL than Design 4c with SF-MPL. This might be the reason why Design 4c and 4d show different HFRs even with the similar conductivities of their respective MPLs.

The contact resistance between the catalyst layer and MPL is also dependent on the material, contact area of contact point, and surface properties [46,47] as well as contact pressure distribution. Therefore, the contact resistance between the corrugated mesh and MPL depends on the number of contact points and spot areas of single contact points, especially in point-to-surface contacts [48] in addition to the electron pathway distance. As described in Section 3.2, the contact between the MPL and corrugated mesh is formed not by the actual line contact but by the aggregate of contact points in the corrugation line, which might need to be considered in the point-to-surface contact case.

4. Conclusions

Here, we have characterized the performance and HFR for corrugated mesh fuel cells, and we demonstrate that the flow field utilizing a corrugated mesh significantly reduces the effects of electrode flooding on their performances. Flow-channel patterns affect the HFR of CCMs and MPLs having sandwich configurations. The conductivities of MPLs are a key factor in the present fuel-cell design to enhance their performances. We also show that MPL rigidity is an important factor in facilitating better contact between the catalyst layer and MPL in the corrugated mesh fuel cells. Finally, we demonstrate a performance of 0.45 V at 3 A cm⁻² and an HFR of 62 mΩ cm⁻² using the combination of a meandering flow pattern and silver-flake MPL. Future studies will involve the calculation of pressure distributions for each MPL under the compression

pressure via 3D-FEM as well as calculations of the resistance in these designs, which involve the experimental measurement of contact resistance and Young's modulus. In addition, since the catalyst layer effect on in-plane conduction in the circuit model (assumption 6) has not been addressed, further investigations of catalyst layer effects on electron transport pathways are planned for the next study. These calculations and experiments are currently ongoing in our lab in order to determine the pressure distribution and resistance associated with each MPL, and will be reported in due course.

Acknowledgments

This work was supported by Fuel Cell Laboratory at Nissan Motor Co., Ltd. We acknowledge Takaaki Arai and Satoshi Takaichi for their dedicated support of this work.

Nomenclature

CB	carbon black
CCM	catalyst-coated membrane
EPDM	ethylene–propylene diene monomer rubber
FEM	finite-element model
GDL	gas-diffusion layer
GF	graphite flake
HFR	high-frequency resistance
IR	current $I \times$ resistance R (ohmic loss)
MEA	membrane-electrode assembly
MPL	microporous layer
PEFC	polymer electrolyte fuel cell
PTFE	polytetrafluoroethylene
RH	relative humidity
SF	silver flake
SS	stainless steel

References

- [1] P.L. Hentall, J.B. Lakeman, G.O. Mepsted, P.L. Adcock, J.M. Moore, J. Power Sources 80 (1999) 235–241.
- [2] K. Jiao, B. Zhou, J. Power Sources 169 (2007) 296–314.
- [3] C. Bao, M. Ouyang, B. Yi, Int. J. Hydrogen Energy 31 (2006) 1879–1896.
- [4] T.V. Nguyen, ECS Trans. 3 (2006) 1171–1180.
- [5] Transitions to Alternative Transportation Technologies—a Focus on Hydrogen, The National Academies Press, Washington, D.C., 2008.
- [6] C.C. Chan, Proc. IEEE 90 (2002) 247–275.
- [7] M. Arita, Fuel Cells 2 (2002) 10–14.
- [8] X.G. Yang, F.Y. Zhang, A.L. Lubawy, C.Y. Wang, Electrochem. Solid State Lett. 7 (2004) A408–A411.
- [9] J.T. Pukrushpan, H. Peng, A.G. Stefanopoulou, J. Dyn. Sys. Meas. Control 126 (2004) 14–25.
- [10] N. Yousfi-Steiner, Ph. Moçotéguy, D. Candusso, D. Hissel, A. Hernandez, A. Aslanides, J. Power Sources 183 (2008) 260–274.
- [11] W. Dai, H. Wang, X.-Z. Yuan, J.J. Martin, D. Yang, J. Qiao, J. Ma, Int. J. Hydrogen Energy 34 (2009) 9461–9478.
- [12] H. Li, Y. Tang, Z. Wang, Z. Shi, S. Wu, D. Song, J. Zhang, K. Fatih, J. Zhang, H. Wang, Z. Liu, R. Abouatallah, A. Mazza, J. Power Sources 178 (2008) 103–117.
- [13] T.A. Zawodzinski Jr., C. Derouin, S. Radzinski, R.J. Sherman, V.T. Smith, T.E. Springer, S. Gottesfeld, J. Electrochem. Soc. 140 (1993) 1041–1047.
- [14] S. Tanaka, T. Shudo, J. Power Sources 248 (2014) 524–532.
- [15] A. Turhan, K. Heller, J.S. Brenizer, M.M. Mench, J. Power Sources 180 (2008) 773–783.
- [16] A. Higier, H. Liu, J. Power Sources 193 (2009) 639–648.
- [17] B.C. Seyfang, Simplification and Investigation of Polymer Electrolyte Fuel Cells Using Micro-Patterned Glassy Carbon Flow Fields, Dissertation No. 18508, ETH Zürich, 2009.
- [18] M. Mathias, J. Roth, J. Fleming, W. Lehnert, in: W. Vielstich, H. Gasteiger, A. Lamm (Eds.), Handbook of Fuel Cells: Fundamentals, Technology and Applications, vol. 3, John Wiley & Sons, New York, 2003.
- [19] F.-Y. Zhang, S.G. Advani, A.K. Prasad, J. Power Sources 176 (2008) 293–298.
- [20] N.S. Siefert, S. Litster, J. Power Sources 196 (2011) 1948–1954.
- [21] H. Yamada, T. Hatanaka, H. Murata, Y. Morimoto, J. Electrochem. Soc. 153 (2006) A1748–A1754.

- [22] ASTM Standard C611, Standard Test Method for Electrical Resistivity of Manufactured Carbon and Graphite Articles at Room Temperature (2010), ASTM International, West Conshohocken, PA, 2003.
- [23] N. Cunningham, M. Lefèvre, G. Lebrun, J.-P. Dodelet, *J. Power Sources* 143 (2005) 93–102.
- [24] M.V. Williams, H.R. Kunz, J.M. Fenton, *J. Electrochem. Soc.* 152 (2005) A635–A644.
- [25] I.S. Hussaini, C.Y. Wang, *J. Power Sources* 195 (2010) 3830–3840.
- [26] E. Aker, K.J. Måløy, A. Hansen, G.G. Batrouni, *Transp. Porous Media* 32 (1998) 163–186.
- [27] Z. Lu, C. Rath, G. Zhang, S.G. Kandlikar, *Int. J. Hydrogen Energy* 36 (2011) 9864–9875.
- [28] A. Turhan, S. Kim, M. Hatzell, M.M. Mench, *Electrochim. Acta* 55 (2010) 2734–2745.
- [29] Y. Wang, S. Al Shakhshir, X. Li, *Appl. Energy* 88 (2011) 2168–2175.
- [30] J.P. Owejan, T.A. Trabold, D.L. Jacobson, D.R. Baker, D.S. Hussey, M. Arif, *Int. J. Heat Mass Transfer* 49 (2006) 4721–4731.
- [31] S.J.C. Cleghorn, D.K. Mayfield, D.A. Moore, J.C. Moore, G. Rusch, T.W. Sherman, N.T. Sisofo, U. Beuscher, *J. Power Sources* 158 (2006) 446–454.
- [32] J.P. Owejan, J.J. Gagliardo, J.M. Sergi, S.G. Kandlikar, T.A. Trabold, *Int. J. Hydrogen Energy* 34 (2009) 3436–3444.
- [33] S. Ge, C.-Y. Wang, *Electrochem. Solid State Lett.* 9 (2006) A499–A503.
- [34] M.L. Perry, T.F. Fuller, *J. Electrochem. Soc.* 149 (2002) S59–S67.
- [35] E. Antolini, R.R. Passos, E.A. Ticianelli, *J. Power Sources* 109 (2002) 477–482.
- [36] P.G. Stampino, L. Omati, C. Cristiani, G. Dotelli, *Fuel Cells* 10 (2010) 270–277.
- [37] S. Kim, M.M. Mench, *J. Electrochem. Soc.* 156 (2009) B353–B362.
- [38] U. Pasaogullari, C.-Y. Wang, K.S. Chen, *J. Electrochem. Soc.* 152 (2005) A1574–A1582.
- [39] J.M. Morgan, R. Datta, *J. Power Sources* 251 (2014) 269–278.
- [40] K.R. Cooper, M. Smith, *J. Power Sources* 160 (2006) 1088–1095.
- [41] M. Ciureanu, R. Roberge, *J. Phys. Chem. B* 105 (2001) 3531–3539.
- [42] S. Asghari, A. Mokmeli, M. Samavati, *Int. J. Hydrogen Energy* 35 (2010) 9283–9290.
- [43] S.J.C. Cleghorn, C.R. Derouin, M.S. Wilson, S. Gottesfeld, *J. Appl. Electrochem.* 28 (1998) 663–672.
- [44] T. Swamy, E.C. Kumbur, M.M. Mench, *J. Electrochem. Soc.* 157 (2010) B77–B85.
- [45] I.N. Sneddon, *Int. J. Eng. Sci.* 3 (1965) 47–57.
- [46] I.V. Zenyuk, E.C. Kumbur, S. Litster, *J. Power Sources* 241 (2013) 379–387.
- [47] T. Swamy, F.E. Hızir, M. Khandelwal, E.C. Kumbur, M.M. Mench, *ECS Trans.* 25 (2009) 15–27.
- [48] R. Holm, *Electric Contacts*, fourth ed., Springer, New York, 1967.